INTERNATIONAL JOURNAL FOR NUMERICAL METHODS IN FLUIDS, VOL. 20, 1–30 (1995)

AN EULER SOLVER FOR THREE-DIMENSIONAL TURBOMACHINERY FLOWS

JOHANNES VASSILIOU SOULIS

Fluid Mechanics/Hydraulics Division, Civil Engineering Department, Democrition University of Thrace,
67100 Xanthi, Greece

SUMMARY

A time-marching finite volume numerical procedure is presented for three-dimensional Euler analysis of turbomachinery flows. The proposed scheme is applied to the conservative form of the Euler equations written in general curvilinear co-ordinates. A simple but computationally efficient grid is constructed. Numerical solution results for three 3D turbine cascade flows have been presented and compared with available measurements as well as with another state-of-the-art 3D Euler analysis numerical solution in order to demonstrate the accuracy and computational efficiency of the analysis method. Also, the predicted results are compared with a 3D potential flow solver and comparison is made with the analytical solution. The proposed method is an accurate and reliable technique for solving the compressible flow equations in turbomachinery geometries.

KEY WORDS Turbomachinery blade rows 3D Euler equations Time-marching finite volume method Body-fitted co-ordinates

INTRODUCTION

The emergence of turbomachines as perhaps the most important means of energy conversion and propulsion is an undisputed fact. Turbomachinery development has been largely conditioned by the improvements achieved in component efficiencies. Design and performance estimation of compressors and turbines has been based, and will continue to be so, almost completely on the understanding of the behaviour of fluid flow passing through the blade rows. However, turbomachinery flow passages are very complex geometrically, while the flow displays significant unsteady and viscous behaviour.

In the past several years significant advances have been made in computational fluid dynamics applied to turbomachinery flows. Although efficient algorithms are now available to integrate the Navier–Stokes equations, this appears to be still a formidable task for purposes of practical applications. In the complex turbomachine environment the prediction accuracy of such viscous flow calculations is limited by the limitations of turbulence modelling. Mixing length eddy viscosity models are by far the most commonly used method.[1]

The numerical solution of 3D inviscid, compressible flow equations is of practical interest in the design of turbomachinery components. Inviscid flow equations are numerically treated in two distinct categories, namely Euler solvers and potential flow solvers. Potential methods do not appear to have been widely used for design purposes. Nowadays 3D Euler solvers are well developed and are available for routine turbomachinery calculations. Several of these dealing with internal and external flows are described by Hirsch.[2]

CCC 0271–2091/95/010001–30

Received March 1994
Accepted June 1994

Euler solvers for 3D turbomachinery flows have been reported as early as 1974 by Denton,[3] who developed an explicit time-marching method. His widely accepted method employs an opposed difference scheme in order to solve the 3D Euler equations. The scheme uses upwind differencing for fluxes of mass and momenta, but downwind differences for pressures in the streamwise direction. In addition, correction factors for each of the physical quantities are applied in the streamwise direction. The method is of the finite volume type. Accurate and efficient 3D Euler equation numerical solution techniques were presented by Shieh and Delaney.[4] The hop-scotch scheme was applied to the conservative form of the Euler equations written in general curvilinear co-ordinates using an O-type grid system. Weber *et al.*[5] presented a 3D Euler analysis on a C-type grid using the well-known Beam–Warming implicit algorithm. Results for a compressor cascade and rotor flows are presented. Arts[6] presented an inviscid flow solution for a transonic axial turbine stage. Holmes and Tong[7] described a 3D Euler solver for turbomachinery blade rows. The algorithm was based on the explicit, four-step, Runge–Kutta finite volume method advocated by Jameson. The solver was tested on turbine nozzles, turbine rotors, centrifugal compressor rotors, fans and propellers.

The objective of this paper is to outline an accurate and efficient numerical procedure for simulating the time-averaged 3D flow field within a typical cascade of turbomachinery blades. The main scope was to calculate flows through all types of turbomachines (axial, mixed, radial) no matter how complex their geometry may be. The proposed scheme has several advantages:

1. The grid used is the simplest possible formation for numerical calculations in turbomachinery blade rows. Leading and trailing edge flow regions do not need special numerical treatment.
2. The conservative form of the equations is written in general curvilinear co-ordinates, thus enabling complex geometry turbomachinery blade rows to be efficiently analysed.
3. The calculated mass flows into and out of the blade row are matched. The net momentum flux into the blade rows balances the net pressure force acting on the blade row. The energy flux is conserved.
4. The boundary conditions are easily and accurately satisfied.
5. The time integration numerical procedure is a straightforward method requiring minimal algorithm coding.
6. Artificial viscosity is provided via a simple pressure correction formula.

For the time being applications are restricted to stationary blade rows, although the numerical algorithm has been developed and presented in this paper to include rotating blade rows. Also, the applied test cases refer to the NACA 34 aerofoil section series, thus enabling the calculated flow results to be properly evaluated by comparing them with available measurements. Numerical solution results for three 3D turbomachinery flows, namely a thick–thin–thick aerofoil, a thick–thin aerofoil and an inclined aerofoil, are presented and compared with available experimental and other numerical data in order to demonstrate the predictive capabilities of the method.

The computer code development was done in the Computation Laboratory of the Fluid Mechanics/Hydraulics Division, Civil Engineering Department, Democrition University of Thrace during the academic years 1991–1993. Near-future application will include an extension of the current code to predict the three-dimensional, viscous flow in hydraulic turbines and pumps and eventually the prediction of three-dimensional free surface flows around hydraulic structures.

GOVERNING FLOW EQUATIONS

The basic equations governing the flow within the impeller of any turbomachine are derived from the principles of conservation of mass, momentum and energy. It is convenient to write the 3D Euler equations in a cylindrical polar co-ordinate system (z, θ, r) which is attached to a rotating or stationary blade row. These equations are expressed in conservation form as

$$-\frac{\partial(r\rho)}{\partial t} = \frac{\partial(r\rho u)}{\partial z} + \frac{\partial[\rho(v - r\Omega)]}{\partial \theta} + \frac{\partial(r\rho w)}{\partial r}, \tag{1}$$

$$-\frac{\partial(r\rho u)}{\partial t} = \frac{\partial[r(\rho u^2 + p)]}{\partial z} + \frac{\partial[\rho(v - r\Omega)u]}{\partial \theta} + \frac{\partial(r\rho uw)}{\partial r}, \tag{2}$$

$$-\frac{\partial(r\rho v)}{\partial t} = \frac{\partial(r\rho uv)}{\partial z} + \frac{\partial[\rho(v - r\Omega)v + p]}{\partial \theta} + \frac{\partial(r\rho vw)}{\partial r} + \rho vw, \tag{3}$$

$$-\frac{\partial(r\rho w)}{\partial t} = \frac{\partial(r\rho uw)}{\partial z} + \frac{\partial[\rho(v - r\Omega)w]}{\partial \theta} + \frac{\partial[r(\rho w^2 + p)]}{\partial r} - (p + \rho v^2), \tag{4}$$

$$-\frac{\partial(r\rho e)}{\partial t} = \frac{\partial[r(\rho e + p)u]}{\partial z} + \frac{\partial[(\rho e + p)v - e\rho r\Omega]}{\partial \theta} + \frac{\partial[r(\rho e + p)w]}{\partial r}, \tag{5}$$

where z, θ and r are the axial, tangential and radial directions respectively, t is the time, ρ is the density, u, v and w are the absolute velocity components along the z-, θ- and r-directions respectively, p is the pressure of the fluid, Ω is the rotational speed of the impeller and e is the total internal energy given by the equation

$$e = \frac{p}{\rho(\gamma - 1)} + \tfrac{1}{2}(u^2 + v^2 + w^2), \tag{6}$$

where γ is the ratio of the specific heats. The unknowns of the problem are the six physical quantities u, v, ρ, p and e. No assumption is made about the geometry of the blade row, but the associated hub and casing surfaces are assumed to be surfaces of revolution. The problem must be closed with a complete specification of the boundary conditions.

Upstream conditions

The stagnation pressure and temperature of the inlet flow are assumed to be constant throughout the flow field; two inlet flow angles must be specified, one for the blade-to-blade and the other for the meridional plane. If instead of the inlet flow angles the pitchwise velocity and spanwise angle are specified, then blade rows with supersonic inlet flow can be calculated.

Downstream conditions

The static pressure is set on the hub surface and the radial pressure distribution is determined from the simple radial equilibrium equation

$$\frac{\partial p}{\partial r} = \frac{\rho v^2}{r}. \tag{7}$$

Body surface conditions

In inviscid flow conditions the flow is tangent to a wall surface, so the flow normal to the blade suction or pressure and/or to the endwall surfaces is zero, i.e.

$$q_n = 0. \tag{8}$$

In internal flow configuration problems the inherent corner formation between hub or casing and suction or pressure surfaces requires special treatment. In turbomachinery flows where highly loaded blades and curved hub or casing surfaces are frequently encountered, the accurate description of the solid boundaries is paramount to obtain satisfactory results.

Periodical boundaries

Periodicity conditions are applied to the extensions from the blade surfaces, requiring the velocities to be identical at corresponding points of two successive periodic planes.

COMPLEX GEOMETRY MESH GENERATION

A complex grid system was developed and implemented on the main numerical method to allow cascade flows for blades of variable chord, twist and cross-section to be calculated. An example of a complex geometry is shown in Figure 1. Blade cross-sections are read at various radial (spanwise) positions. Each input cross-section is obtained from axial, suction surface and blade thickness co-ordinates, allowing the blade shape to be properly described. Hub and casing radial co-ordinates along the machine axis are also provided as an input to the computer code. Input cross-sections are interpolated to calculate the axial, suction surface and blade thickness

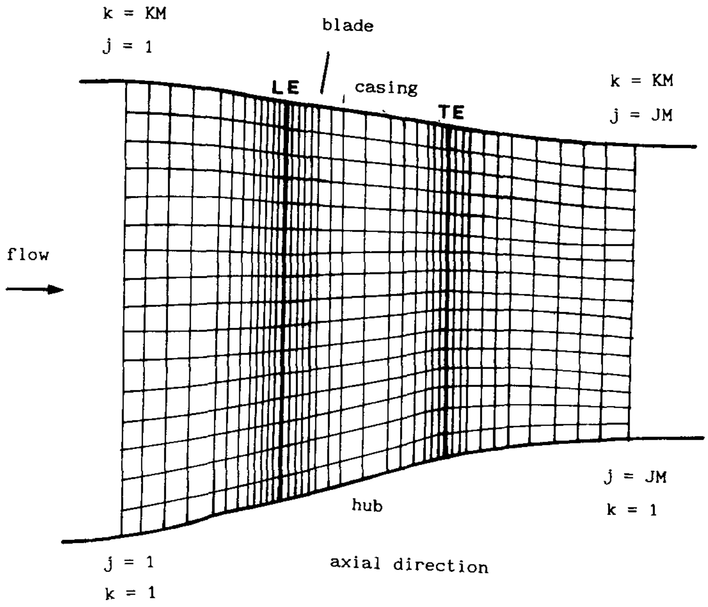

Figure 1. Intersection of the 3D grid with the meridional plane

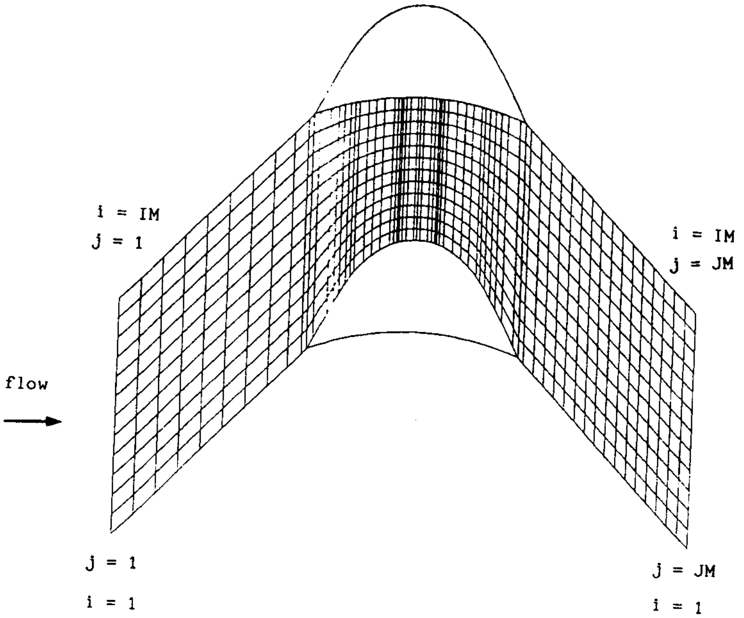

Figure 2. Intersection of the 3D grid with the blade-to-blade plane

meridional grid points which are uniformly spaced in the r-direction. For linear cascade geometries the hub and tip radii are set to large values such that the difference between them is the blade span (height), their ratio being close to unity, while the angular blade distance $2\pi/N$ (N is the number of blades in the row) multiplied by the mean span radius yields the cascade pitch.

The calculation of the blade-to-blade grid points containing the tangential and axial variations is based on simple interpolations between the blade suction and pressure surfaces. Axial points need not be equally spaced. Figure 2 shows the intersection of the 3D grid with the blade-to-blade plane. A provision is made for the pitch variation along the radial direction for annular cascades.

The chosen grid is the simplest possible formation for numerical calculations in cascade fluid dynamics problems. Use of pitchwise lines greatly simplifies the application of the periodic boundary properties between the bounding quasi-streamlines of the blade passage. However, the numerical scheme can be used with any grid formation, which need not be uniformly spaced in any co-ordinate direction. The grid is not restricted to that shown. Any mesh generation technique can be adopted provided that grid periodicity is maintained. Leading and trailing edges require special numerical treatment. The problem can be overcome by fitting more grid points where appropriate.

TRANSFORMATION EQUATIONS

The discrete approximation to the governing flow equation has been developed by dividing the physical domain into cuboid cells which can be defined arbitrarily to produce surface-fitted grids, the structure of which follows the turbomachinery internal configuration. Once this has been achieved, a transformation is introduced through which cuboids of the physical domain

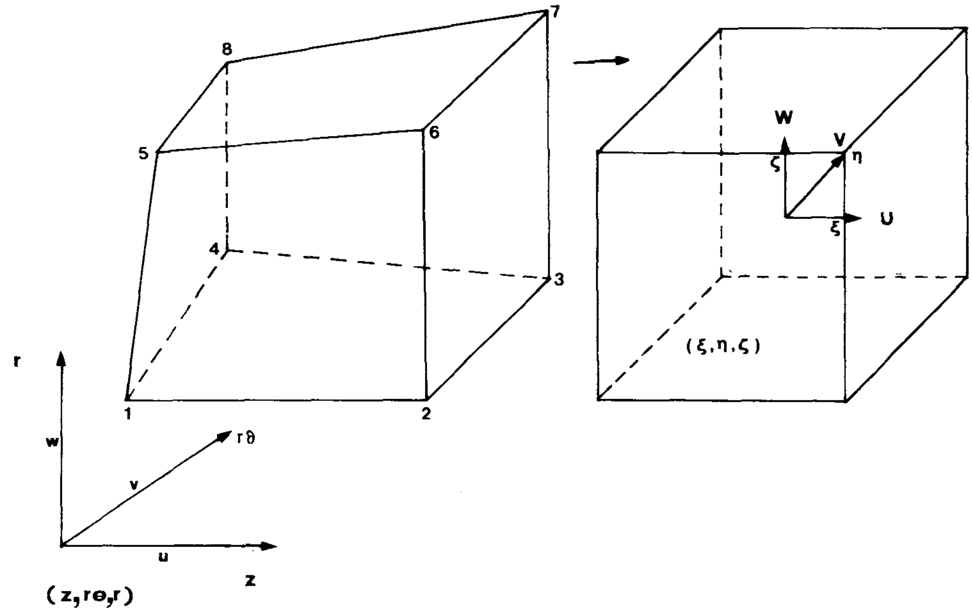

Figure 3. Distorted cubes of the physical domain are mapped into cubes of the computational domain

are mapped into cubes of the computational domain; see Figure 3. The transformation from global (z, θ, r) co-ordinates to local (ξ, η, ζ) co-ordinates can be expressed as[8]

$$z = \sum_{i=1}^{8} N_i z_i, \qquad \theta = \sum_{i=1}^{8} N_i \theta_i, \qquad r = \sum_{i=1}^{8} N_i r_i, \tag{9}$$

where N_i are the first-order, linear shape functions associated with the cuboid nodes. The use of first-order shape functions has been determined by the necessity to restrict the complexity of the numerical code, which is inherent to almost all 3D computational methods.

Thus, in order to numerically solve the system of governing flow equations (1)–(6) on a body-fitted grid system, the equations are transformed to an arbitrary curvilinear system $\xi(z, \theta, r)$, $\eta(z, \theta, r)$ and $\zeta(z, \theta, r)$ using the chain rule:[9]

$$-\frac{\partial(rJ^{-1}\rho)}{\partial t} = \frac{\partial(rJ^{-1}\rho U)}{\partial \xi} + \frac{\partial(rJ^{-1}\rho V)}{\partial \eta} + \frac{\partial(rJ^{-1}\rho W)}{\partial \zeta}, \tag{10}$$

$$-\frac{\partial(rJ^{-1}\rho u)}{\partial t} = \frac{\partial[rJ^{-1}(\rho uU + \xi_z p)]}{\partial \xi} + \frac{\partial[rJ^{-1}(\rho uV + \eta_z p)]}{\partial \eta} + \frac{\partial[rJ^{-1}(\rho uW + \zeta_z p)]}{\partial \zeta}, \tag{11}$$

$$-\frac{\partial(rJ^{-1}\rho v)}{\partial t} = \frac{\partial[rJ^{-1}(\rho vU + \xi_\theta p/r)]}{\partial \xi} + \frac{\partial[rJ^{-1}(\rho vV + \eta_\theta p/r)]}{\partial \eta} + \frac{\partial[rJ^{-1}(\rho vW + \zeta_\theta p/r)]}{\partial \zeta} + J^{-1}\rho vw, \tag{12}$$

$$-\frac{\partial(rJ^{-1}\rho w)}{\partial t}=\frac{\partial[rJ^{-1}(\rho wU+\xi_r p)]}{\partial\xi}+\frac{\partial[rJ^{-1}(\rho wV+\eta_r p)]}{\partial\eta}$$

$$+\frac{\partial[rJ^{-1}(\rho wW+\zeta_r p)]}{\partial\zeta}-J^{-1}(\rho v^2+p), \tag{13}$$

$$-\frac{\partial\{rJ^{-1}\rho e\}}{\partial t}=\frac{\partial\{rJ^{-1}[(\rho e+p)U+\xi_\theta p(r\Omega)/r]\}}{\partial\xi}+\frac{\partial\{rJ^{-1}[(\rho e+p)V+\eta_\theta p(r\Omega)/r]\}}{\partial\eta}$$

$$+\frac{\partial\{rJ^{-1}[(\rho e+p)W+\zeta_\theta p(r\Omega)/r]\}}{\partial\zeta}, \tag{14}$$

where U, V and W are the contravariant velocity components in the ξ-, η- and ζ-directions respectively. The inverse Jacobian J^{-1} of the transformation from the physical to the local co-ordinate system is defined as

$$J^{-1}=\begin{bmatrix} z_\xi & z_\eta & z_\zeta \\ \theta_\xi & \theta_\eta & \theta_\zeta \\ r_\xi & r_\eta & r_\zeta \end{bmatrix}. \tag{15}$$

The metrics ξ_z, η_z and ζ_z of equation (11) are

$$\xi_z=(\theta_\eta r_\zeta-r_\eta\theta_\zeta)/J^{-1},\qquad \eta_z=(r_\xi\theta_\zeta-\theta_\xi r_\zeta)/J^{-1},\qquad \zeta_z=(\theta_\xi r_\eta-\theta_\eta r_\xi)/J^{-1}.$$

Similarly the metrics ξ_θ, η_θ and ζ_θ of equation (12) are

$$\xi_\theta=(z_\zeta r_\eta-z_\eta r_\zeta)/J^{-1},\qquad \eta_\theta=(z_\xi r_\zeta-z_\zeta r_\xi)/J^{-1},\qquad \zeta_\theta=(z_\eta r_\xi-z_\xi r_\eta)/J^{-1}, \tag{16}$$

while the metrics ξ_r, η_r and ζ_r of equation (13) are

$$\xi_r=(z_\eta\theta_\zeta-z_\zeta\theta_\eta)/J^{-1},\qquad \eta_r=(z_\zeta\theta_\xi-z_\xi\theta_\zeta)/J^{-1},\qquad \zeta_r=(z_\xi\theta_\eta-z_\eta\theta_\xi)/J^{-1}.$$

The contravariant velocities are related to the physical velocities by the equations

$$U=\xi_z u+(\xi_\theta/r)(v-r\Omega)+\xi_r w, \tag{17}$$

$$V=\eta_z u+(\eta_\theta/r)(v-r\Omega)+\eta_r w, \tag{18}$$

$$W=\zeta_z u+(\zeta_\theta/r)(v-r\Omega)+\zeta_r w. \tag{19}$$

In all the above equations the subscripts z, θ and r refer to partial derivatives.

NUMERICAL ALGORITHM

For a control volume ΔV and for a given time step Δt the transformed governing flow equations (10)–(14) may be written as

$$-\Delta(rJ^{-1}\rho)=[\Delta(rJ^{-1}\rho U)\Delta\eta\Delta\zeta+\Delta(rJ^{-1}\rho V)\Delta\xi\Delta\zeta+\Delta(\rho J^{-1}\rho W)\Delta\xi\Delta\eta]\Delta t/(\Delta\xi\Delta\eta\Delta\zeta) \tag{20}$$

$$-\Delta(rJ^{-1}\rho u)=\{\Delta[rJ^{-1}(\rho uU+\xi_z p)]\Delta\eta\Delta\zeta$$

$$+\Delta[rJ^{-1}(\rho uV+\eta_z p)]\Delta\xi\Delta\zeta+\Delta[rJ^{-1}(\rho uW+\zeta_z p)]\Delta\xi\Delta\eta\}\Delta t/(\Delta\xi\Delta\eta\Delta\zeta), \tag{21}$$

$$-\Delta(rJ^{-1}\rho v) = \{\Delta[rJ^{-1}(\rho v U + \xi_\theta p/r)]\Delta\eta\Delta\zeta + \Delta[rJ^{-1}(\rho v V + \eta_\theta p/r)]\Delta\xi\Delta\zeta$$
$$+ \Delta[rJ^{-1}(\rho v W + \zeta_\theta p/r)]\Delta\xi\Delta\eta\}\Delta t/(\Delta\xi\Delta\eta\Delta\zeta) + J^{-1}\rho v w \Delta t, \qquad (22)$$

$$-\Delta(rJ^{-1}\rho w) = \{\Delta[rJ^{-1}(\rho w U + \xi_r p)]\Delta\eta\Delta\zeta + \Delta[rJ^{-1}(\rho w V + \eta_r p)]\Delta\xi\Delta\zeta$$
$$+ \Delta[rJ^{-1}(\rho w W + \zeta_r p)]\Delta\xi\Delta\eta\}\Delta t/(\Delta\xi\Delta\eta\Delta\zeta) - [J^{-1}(\rho v^2 + p)]\Delta t, \qquad (23)$$

$$-\Delta(rJ^{-1}\rho e) = \{\Delta[rJ^{-1}(\rho e + p)U]\Delta\eta\Delta\zeta + \Delta[rJ^{-1}(\rho e + p)V]\Delta\xi\Delta\zeta$$
$$+ \Delta[rJ^{-1}(\rho e + p)W]\Delta\xi\Delta\eta\}\Delta t/(\Delta\xi\Delta\eta\Delta\zeta). \qquad (24)$$

Figure 4 shows the notation used for flux balancing across a finite volume of the flow field.

Thus for the *mass flux* an XFLUX at point i, j, k is defined as

$$(\text{XFLUX})_{i,j,k} = 0{\cdot}25[(rJ^{-1}\rho U)_{i,j,k} + (rJ^{-1}\rho U)_{i+1,j,k}$$
$$+ (rJ^{-1}\rho U)_{i+1,j,k+1} + (rJ^{-1}\rho U)_{i,j,k+1}]\Delta\eta\Delta\zeta. \qquad (25)$$

The TFLUX at the same point i, j, k is defined as

$$(\text{TFLUX})_{i,j,k} = 0{\cdot}25[(rJ^{-1}\rho V)_{i,j,k} + (rJ^{-1}\rho V)_{i,j,k+1}$$
$$+ (rJ^{-1}\rho V)_{i,j-1,k+1} + (rJ^{-1}\rho V)_{i,j-1,k}]\Delta\xi\Delta\zeta, \qquad (26)$$

while $(\text{RFLUX})_{i,j,k}$ is defined as

$$(\text{RFLUX})_{i,j,k} = 0{\cdot}25[(rJ^{-1}\rho W)_{i,j,k} + (rJ^{-1}\rho W)_{i+1,j,k} + (rJ^{-1}\rho W)_{i,j-1,k}$$
$$+ (rJ^{-1}\rho W)_{i+1,j-1,k}]\Delta\eta\Delta\zeta, \qquad (27)$$

where i, j and k are the point indices in the ξ-, η- and ζ-co-ordinate directions respectively. For

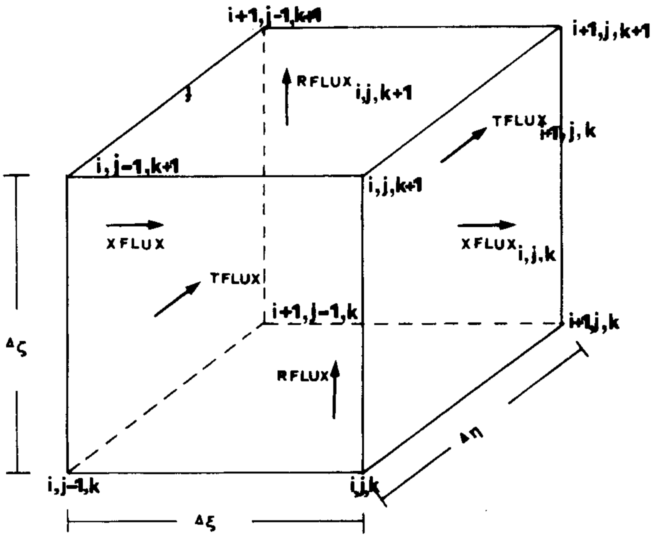

Figure 4. Flux balancing across a finite volume

the ξ-*momentum flux* balance the corresponding $(\mathrm{XFLUX})_{i,j,k}$, $(\mathrm{TFLUX})_{i,j,k}$ and $(\mathrm{RFLUX})_{i,j,k}$ are defined as

$$\begin{aligned}(\mathrm{XFLUX})_{i,j,k} = 0{\cdot}25\{&[rJ^{-1}(\rho uU + \xi_z p)]_{i,j,k} + [rJ^{-1}(\rho uU + \xi_z p)]_{i+1,j,k} \\ &+ [rJ^{-1}(\rho uU + \xi_z p)]_{i+1,j,k+1} + [rJ^{-1}(\rho uU + \xi_z p)]_{i,j,k+1}\}\Delta\eta\Delta\zeta, \end{aligned} \tag{28}$$

$$\begin{aligned}(\mathrm{TFLUX})_{i,j,k} = 0{\cdot}25\{&[rJ^{-1}(\rho uV + \eta_z p)]_{i,j,k} + [rJ^{-1}(\rho uV + \eta_z p)]_{i,j,k+1} \\ &+ [rJ^{-1}(\rho uV + \eta_z p)]_{i,j-1,k+1} + [rJ^{-1}(\rho uV + \eta_z p)]_{i,j-1,k}\}\Delta\xi\Delta\zeta, \end{aligned} \tag{29}$$

$$\begin{aligned}(\mathrm{RFLUX})_{i,j,k} = 0{\cdot}25\{&[rJ^{-1}(\rho uW + \zeta_z p)]_{i,j,k} + [rJ^{-1}(\rho uW + \zeta_z p)]_{i+1,j,k} \\ &+ [rJ^{-1}(\rho uW + \zeta_z p)]_{i+1,j,k+1} + [rJ^{-1}(\rho uW + \zeta_z p)]_{i+1,j-1,k}\}\Delta\eta\Delta\zeta. \end{aligned} \tag{30}$$

Similar expressions hold for the XFLUX, TFLUX and RFLUX fluxes of the η-*momentum*, ζ-momentum and *energy equations*. The terms $\Delta(rJ^{-1}\rho U)$, $\Delta(rJ^{-1}\rho V)$ and $\Delta(rJ^{-1}\rho W)$ of the RHS of equation (20) are defined as

$$\Delta(rJ^{-1}\rho U) = (\mathrm{XFLUX})_{i,j,k} - (\mathrm{XFLUX})_{i,j-1,k}, \quad i = 1,IM, \quad j = 1,JM, \quad k = 1,KM, \tag{31}$$

$$\Delta(rJ^{-1}\rho V) = [(\mathrm{TFLUX})_{i+1,j,k} - (\mathrm{TFLUX})_{i-1,j,k}]0{\cdot}5, \quad i = 2,IMM1, \quad j = 1,JM, \quad k = 2,KMM1, \tag{32}$$

$$\Delta(rJ^{-1}\rho W) = [(\mathrm{RFLUX})_{i,j,k+1} - (\mathrm{RFLUX})_{i,j,k-1}]0{\cdot}5, \quad i = 2,IMM1, \quad j = 1,JM, \quad k = 2,KMM1. \tag{33}$$

The index i ranges from 1 to IM along the tangential direction. $IMM1$ is equal to $IM - 1$; see Figure 2. The index j ranges from 1 to JM along the axial direction; see Figures 1 and 2. The index k ranges from 1 to KM along the radial direction; see Figure 1. $KMM1$ is equal to $KM - 1$. Similar differencing is adopted for the RHS differences of equations (21)–(24). Partial derivatives of, say, z at the cell centres $\xi = \eta = \zeta = 0$ are calculated by formulae such as

$$z_\xi = 0{\cdot}25[z_{i,j,k} + z_{i+1,j,k} + z_{i+1,j,k+1} + z_{i,j,k+1} - (z_{i,j-1,k} + z_{i+1,j-1,k} + z_{i+1,j-1,k+1} + z_{i,j-1,k+1})], \tag{34}$$

$$z_\eta = 0{\cdot}25[z_{i+1,j,k} + z_{i+1,j,k+1} + z_{i,j-1,k+1} + z_{i+1,j-1,k} - (z_{i,j,k} + z_{i,j,k+1} + z_{i,j-1,k+1} + z_{i,j-1,k})], \tag{35}$$

$$\begin{aligned}z_\zeta = 0{\cdot}25[&z_{i+1,j,k+1} + z_{i+1,j,k+1} + z_{i,j-1,k+1} + z_{i+1,j-1,k+1} - (z_{i+1,j,k} + z_{i+1,j,k} \\ &+ z_{i,j-1,k} + z_{i+1,j-1,k})],\end{aligned} \tag{36}$$

with similar expressions for the partial derivatives of θ and r with respect to ξ, η and ζ respectively. The spatial increments $\Delta\xi$, $\Delta\eta$ and ζ are equal to unity and therefore have been omitted. Note that the first-order differencing scheme used to calculate the metrics, equations (34)–(36), is identical to the scheme used to approximate the axial spatial derivatives in the governing system of equations, equation (31). The same principles hold for the tangential and radial spatial derivatives but only for the rows used to describe the solid boundaries and corners. Inside the main flow field the spatial tangential and radial derivatives utilize second-order accuracy; see equations (32) and (33). If the grid conservation law is not satisfied, the numerical solution scheme may not reproduce uniform flow conditions. Such conditions were not encountered during the computer code development or during the computation of the tested flow cases. All information regarding turbomachinery geometries and associated metrics is calculated at once and their values are stored for future computations. Linear extrapolations are used to determine geometry values at rows immediately outside the main flow field. Now all fluxes and partial derivatives may be used in equations (20)–(24) to obtain the changes $\Delta(rJ^{-1}\rho)$, $\Delta(rJ^{-1}\rho u)$, $\Delta(rJ^{-1}\rho v)$, $\Delta(rJ^{-1}\rho w)$ and $\Delta(J^{-1}\rho e)$ and thereafter the values of ρ, u, v, w and e for the time step under consideration.

When an attempt was made to pass all changes directly into the old values in order to calculate the new ones, it was found necessary to utilize two different amplification factors,[10] a factor C_1 for the estimation of ρ and a factor C_2 for the e, u, v and w. The numerical procedure is as follows:

$$(rJ^{-1}\Phi)^{n+1}_{i,j,k} = (rJ^{-1}\Phi)^{n}_{i,j,k} + \mathrm{Corr}^{n+1}_{i,j,k}, \tag{37}$$

where Φ stands for ρ and

$$\mathrm{Corr}^{n+1}_{i,j,k} = \frac{\Delta(rJ^{-1}\Phi)^{n+1}_{i,j,k}}{1 + C_1\Delta(rJ^{-1}\Phi)^{n+1}_{i,j,k}}, \tag{38}$$

with $C_1 = 0{\cdot}1/\rho^{0}_{1,1,1}$; also,

$$(rJ^{-1}\Psi)^{n+1}_{i,j,k} = (rJ^{-1}\Psi)^{n}_{i,j,k} + \mathrm{Corr}^{n+1}_{i,j,k}, \tag{39}$$

where Ψ stands for e, u, v or w and

$$\mathrm{Corr}^{n+1}_{i,j,k} = \frac{\Delta(rJ^{-1}\Psi)^{n+1}_{i,j,k}}{1 + C_2\Delta(rJ^{-1}\Psi)^{n+1}_{i,j,k}}, \tag{40}$$

with $C_2 = 0{\cdot}025/(\rho u)^{0}_{1,1,1}$. The upper index '$n$' denotes the computed result of the previous iteration, while the upper index 'o' denotes the initially estimated flow property. The numerical scheme was found to be stable over a wide range of considered values of C_1 and C_2. For all governing flow equations $\mathrm{Corr}^{n+1}_{i,j,k}$ is calculated as

$$\mathrm{Corr}^{n+1}_{i,j,k} = C_3\,\mathrm{Corr}^{n+1}_{i,j,k} + 0{\cdot}5(1{\cdot}0 - C_3)(\mathrm{Corr}^{n+1}_{i,j-1,k} + \mathrm{Corr}^{n+1}_{i,j+1,k}). \tag{41}$$

Numerical experimentation has shown that the value of the factor C_3 should be greater than 0·5. A typical value for C_3 was set equal to 0·8. In order to maintain numerical stability,[11] the pressure is taken from the downwind face of the cell. The downwinded pressure is corrected by the addition of an extra pressure. Thus

$$p_{i,j,k} = p_{i,j,k} + \mathrm{pcor}_{i,j,k}, \tag{42}$$

where $\mathrm{pcor}_{i,j+1,k}$ is the pressure correction. This additional pressure is calculated from

$$\mathrm{pcor}_{i,j,k} = 0{\cdot}5C_4(p_{i,j-1,k} - p_{i,j+1,k}), \tag{43}$$

where C_4 is a factor, typically 0·1. Finally, the value of $\mathrm{pcor}_{i,j,k}$ in equation (43) is relaxed before it is incorporated into equation (42). A typical relaxation factor was found to be 0·1. In steep pressure gradients, e.g. in shock wave flow regions, the value of C_4 is related to the density gradient $\Delta\rho/\rho$. Outside this region C_4 takes its usual value. It must be emphasized that the corrected pressure, equation (42), is applied to each of the ξ-, η- and ζ- momentum equations and not the true pressure. Of course, for all XFLUXs (continuity, ξ-momentum, η-momentum, z-momentum) upwinded values for velocities and energies are used, while the pressure is taken from the downwind face of the finite volume involved. Thus the proper expression for equation (25) becomes

$$(\mathrm{XFLUX})_{i,j,k} = 0{\cdot}25[(rJ^{-1}\rho U)_{i,j-1,k} + (rJ^{-1}\rho U)_{i+1,j-1,k} + (rJ^{-1}\rho U)_{i+1,j-1,k+1} + (rJ^{-1}\rho U)_{i,j-1,k+1}]\Delta\eta\Delta\zeta, \tag{44}$$

while for the ξ-momentum, equation (28), all indices regarding the products $\rho u U$ refer to the $i, j-1, k$ grid point and not the i, j, k one. All indices for the fluxes TFLUX and RFLUX remain unchanged. Finally the index j of equation (31) has been shifted by one so as to be compatible with the upwinding procedure. Thus equation (31) becomes

$$\Delta(rJ^{-1}\rho U) = (\mathrm{XFLUX})_{i,j+1,k} - (\mathrm{XFLUX})_{i,j,k}. \tag{45}$$

As with all time-marching methods, the theoretical maximum stable time step Δt is determined by the CFL criterion

$$\Delta t = C_5 \frac{\Delta s}{c}, \tag{46}$$

where c is the inlet stagnation speed of sound, Δs is the minimum of $(\Delta z)s$, $\Delta(r\theta)s$ and $(\Delta r)s$, while C_5 is a factor (its value is determined after numerical experimentation) helping to stabilize the solution, typically 0·1. To accelerate the solution, it was found necessary to use variable time steps. Then the exact value of each Δt depends upon the geometry of the particular finite volume under consideration. High values of the factor C_5 ($>0{\cdot}3$ depending upon the ratio $\Delta s/c$) may lead the numerical convergence procedure into instability and later on into numerical failure due to the violation of the CFL criterion. In contrast, small values of C_5 may considerably delay the solution convergence. Numerical experimentation is also needed for the proper selection of C_5 in relation to C_1 and C_2, since otherwise the convergence procedure may also be seriously delayed or end up in a wrong solution (mass is not conserved). These considerations apart, the numerical procedure proved to be reliable enough provided that the tested turbomachinery geometries were smooth.

The governing flow equations are solved in the order mass, energy, ξ-momentum, η-momentum and ζ-momentum. The input data for the description of the physical quantities and geometry have been kept to a minimum. Thereafter the computational grid is easily formed. More grid points are used in the regions of high-curvature geometry (leading or trailing edge); see Figures 1 and 2. An initial proper distribution of pressure, density and velocity components is crucial for achieving fast convergence. The new density is calculated from the continuity equation. Using old velocities and density, the new energy field is calculated. Thereafter the pressure is calculated using old velocities but new density and energy. Boundary conditions are applied for the inlet and outlet sections. The ξ-, η- and ζ-momentum equations are solved to yield the new axial, tangential and radial velocities using old u, v, w, U, V, W and ρ but new p. Proper boundary conditions are applied to solid and periodic surfaces. Once a steady state solution is obtained, the sum of mass, energy and momentum fluxes over the six faces of each cell will be zero and hence the conservation equations are satisfied.

A convergence criterion based on the percentage change on the average flow field velocity over the previous iteration values is checked. If it has not been satisfied, the iterations continue till the average value drops to 0·00005%. The 0·00005% value proved to be a very satisfactory criterion. Numerical experimentation has shown that if this number was set equal to a higher value (one order of magnitude), the results would also have been acceptable from an engineering

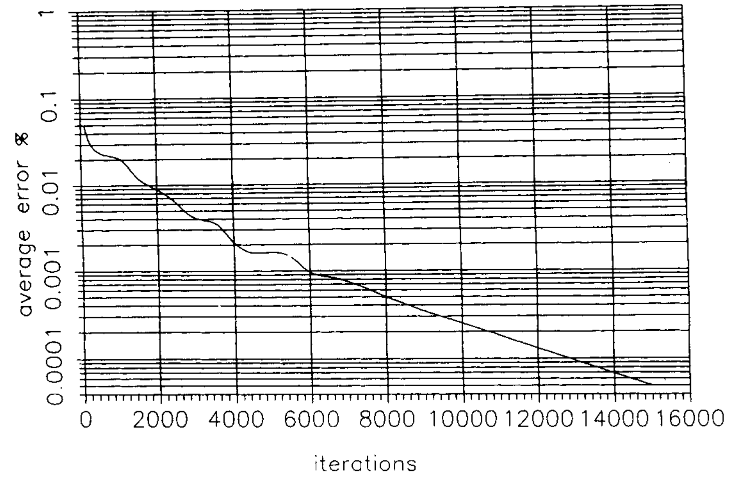

Figure 5. Solution convergence for the thick–thin–thick aerofoil

point of view. A second convergence criterion is also applied based on the percentage change in the maximum axial velocity over the previous iteration values. However, this criterion proved to be unsatisfactory in cases where the flow field produced local instabilities, which is a frequent occurrence in high-curvature geometries.

The total number of iterations required to achieve the above convergence was about 12,000 (see Figure 5), depending upon the geometric complexity, initial pressure distribution, type of flow (subsonic, transonic or supersonic) and grid density. The computational grid was formed by finite volumes of $\Delta z : \Delta(r\theta) : \Delta r \cong 1:1:1$. Grid reduction tests for nearly all applied test cascade cases have shown that $\Delta z : \Delta(r\theta) : \Delta r$ ratios above a certain value do not essentially alter the Mach number distribution (maximum error less than 0·5%). A total of 40 three-dimensional arrays were incorporated and the maximum number of grid points of each array was set equal to 50 × 100 × 50 (tangential × axial × radial).

Incompressible (water) flow through turbines and pumps in either rotating or stationary turbomachinery elements or through other internal flow configuration systems, e.g. draft tubes, is a near-future extension of the current research work.

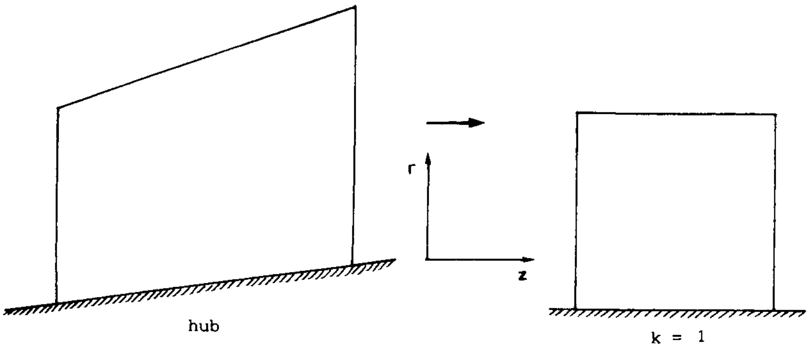

Figure 6. Boundary finite volume for the hub (casing) surfaces

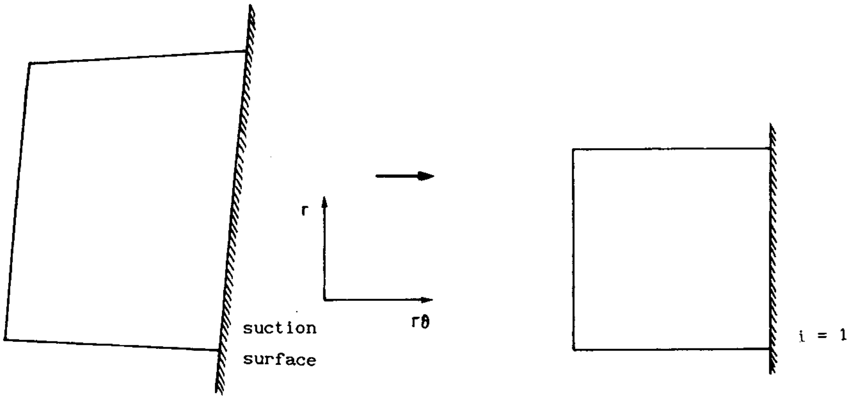

Figure 7. Boundary finite volume for the suction (pressure) surfaces

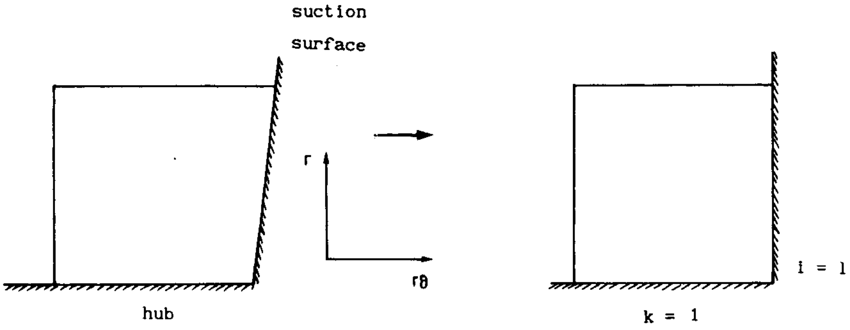

Figure 8. Corner boundary finite volumes

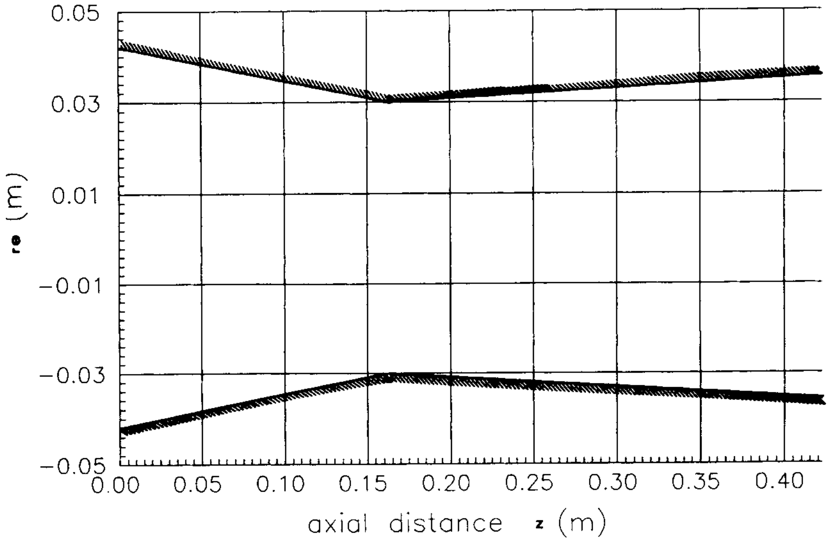

Figure 9. Geometry of the converging–diverging nozzle

BOUNDARY CONDITIONS

Hub, casing, suction and pressure surface flows

Figure 6 shows the boundary cell of the first computational plane $k = 1$ (hub) of the flow field. It is possible for a cell on the hub plane to be bounded on more than one face by solid boundaries (suction or pressure). When the flux balance is established on the secondary cell i, j, k, the mass flux through the solid body (hub) must be zero, i.e. $W_{i,j,1} = 0$. The treatment of the casing surface ($k = KM$) requires $W_{i,j,KM} = 0$. Similarly the mass flux through the suction surface ($i = 1$) must be zero, i.e. $V_{1,j,k} = 0$ (see Figure 7), while across the pressure surface ($i = IM$) $V_{IM,j,k} = 0$. Figure 8 shows a cell bounded on two faces by solid boundaries. When the mass flux balance is established on the cell, the flux through the solid body of the hub ($k = 1$) and that of the pressure surface ($i = 1$) must both be zero, i.e. $W_{1,j,1} = 0$ and $V_{1,j,1} = 0$.

Periodic boundaries, inlet and exit

It is assumed that the flow is identical in each blade passage of the turbomachine, so only one passage needs to be considered. The inlet and outlet flow regions are divided by imaginary surfaces extended upstream and downstream from the blade leading and trailing edges respectively. These extensions are located at angular intervals $\Delta\theta = 2\pi/N$. The application of periodic boundaries along the imaginary surfaces requires that all flow properties are identical at corresponding grid points. This condition is easily applied. At the upstream boundary the inlet total pressure p_{01}, total temperature T_{01} and radial and tangential velocity components are specified for subsonic flow. Non-uniform radial distributions of any of these properties can also be applied. For supersonic inflow (not tested) it is convenient to hold the tangential velocity

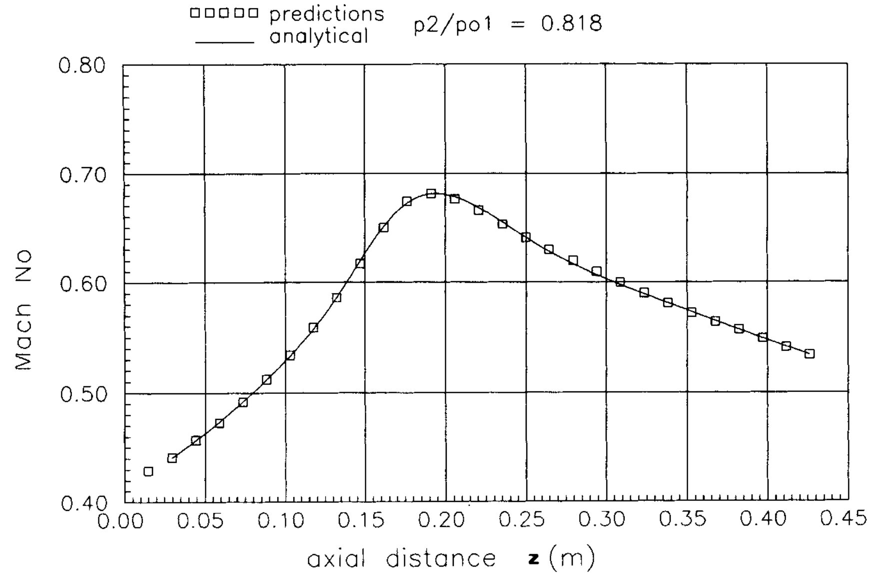

Figure 10. Comparison between current method predictions and analytical solution for the Mach number distribution for the converging–diverging nozzle

component fixed and to allow the inlet direction to vary. The static pressure is calculated from the interior flow field. Thus

$$p_{i,1,k}^{n+1} = (1{\cdot}0 - C_6)p_{i,1,k}^{n} + C_6 p_{i,2,k}^{n+1}, \tag{47}$$

where C_6 is typically 0·25. Thereafter the absolute velocity is calculated using isentropic relationships and stagnation values. This enables the inlet velocity and contravariant velocity components to be properly calculated. At the downstream boundary the static pressure distribution is determined from the simple radial equilibrium equation (7). This pressure distribution is imposed as a boundary condition at the next time step. All other flow properties, i.e. velocity components and internal energy, are extracted from the interior flow region using linear extrapolations.

COMPUTATIONAL RESULTS AND DISCUSSION

The numerical scheme introduced in the previous sections is evaluated in this section by presenting a range of numerically computed examples, including subsonic, shocked and shock-free flow test cases. Comparisons are made against a wide range of other solutions, analytical or numerical, and with available experimental data in various geometry configurations. For the time being applications are restricted to stationary blade rows, although the numerical algorithm has been developed and presented in this paper to include rotating blade rows. Also, the applied test cases refer to the NACA 34 aerofoil section series, thus enabling the calculated flow results to be properly evaluated by comparing them with available measurements.

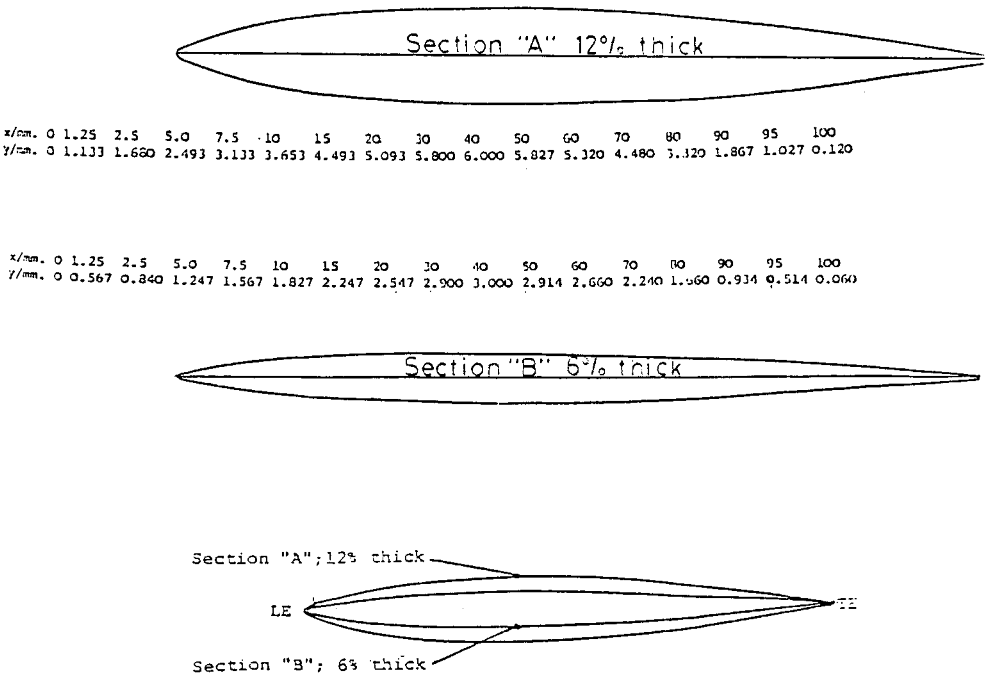

x/mm.	0	1.25	2.5	5.0	7.5	10	15	20	30	40	50	60	70	80	90	95	100
y/mm.	0	1.133	1.680	2.493	3.133	3.653	4.493	5.093	5.800	6.000	5.827	5.320	4.480	3.120	1.867	1.027	0.120

x/mm.	0	1.25	2.5	5.0	7.5	10	15	20	30	40	50	60	70	80	90	95	100
y/mm.	0	0.567	0.840	1.247	1.567	1.827	2.247	2.547	2.900	3.000	2.914	2.660	2.240	1.560	0.934	0.514	0.060

Figure 11. Dawes aerofoil thin and thick sections; all dimensions in millimetres

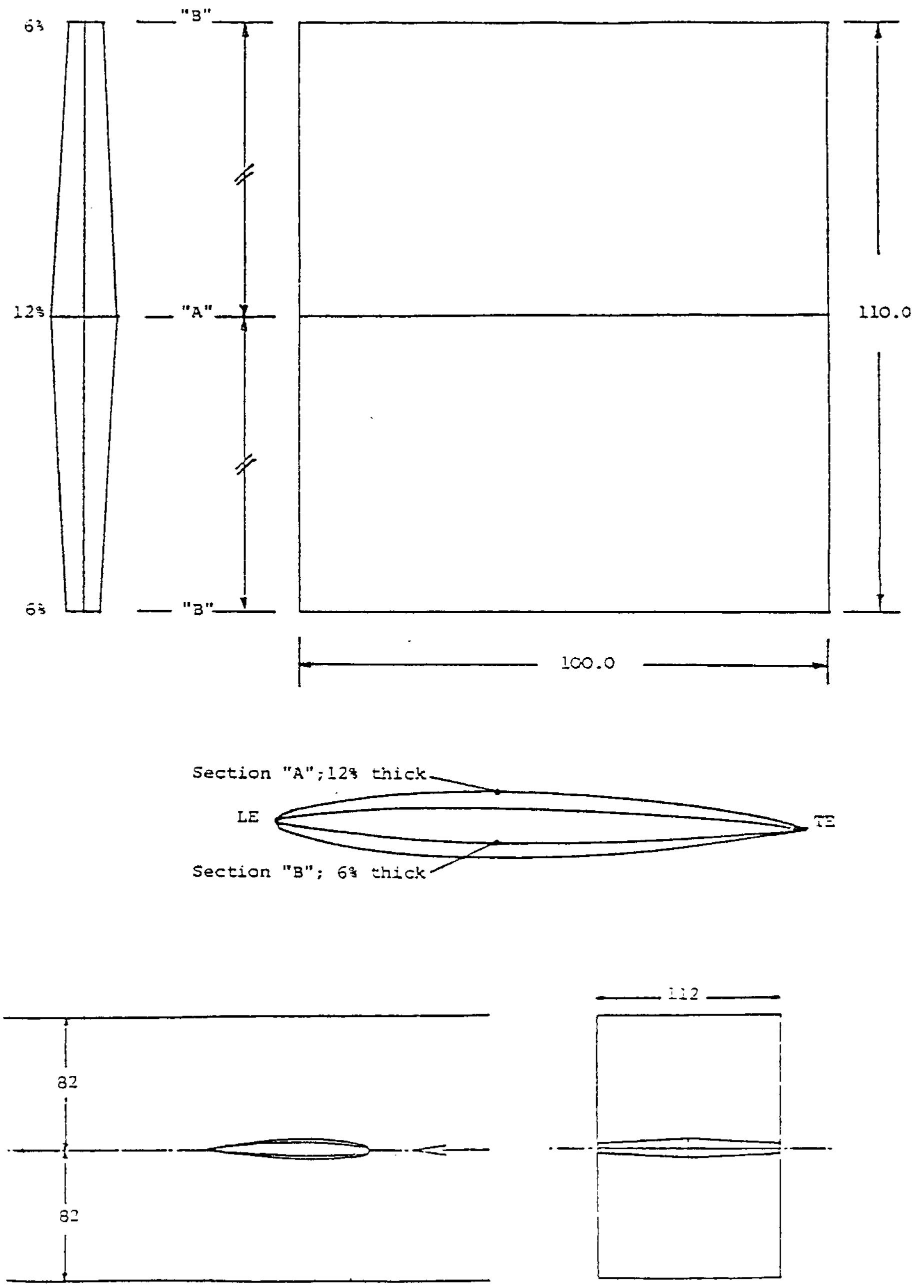

Figure 12. Dawes 'thin–thick–thin' aerofoil and working section arrangements; all dimensions in millimetres

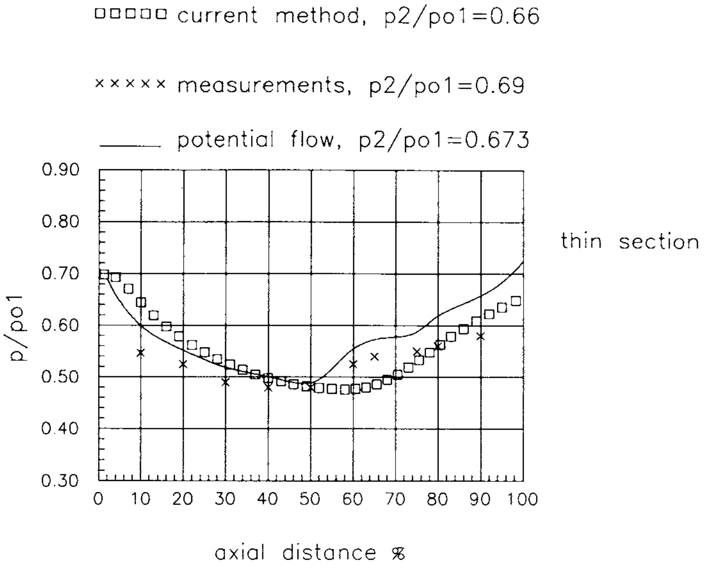

Figure 13. Comparison of blade pressure distribution between current method predictions, potential flow predictions and measurements on the thin section of the 'thin–thick–thin' aerofoil

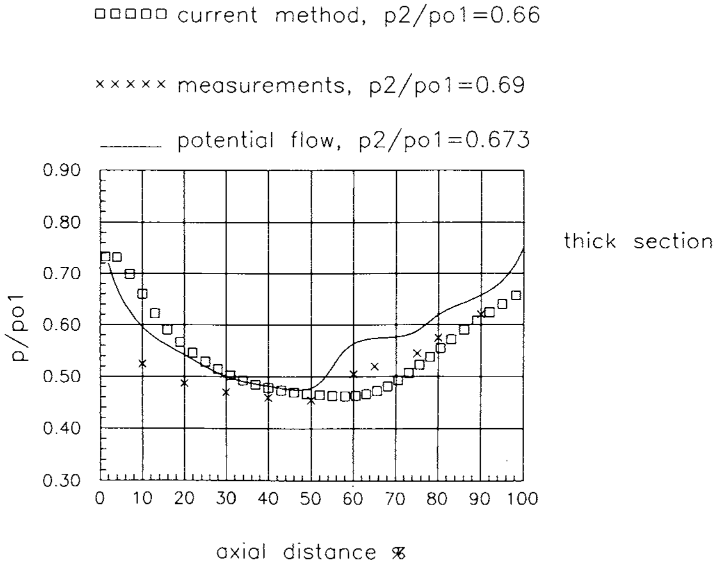

Figure 14. Comparison of blade pressure distribution between current method predictions, potential flow predictions and measurements on the thick section of the 'thin–thick–thin' aerofoil

Converging–diverging nozzle

In order to test the basic numerical scheme, a convergent–divergent nozzle is examined. Figure 9 shows the nozzle geometry. The basic feature of the nozzle under investigation is the abrupt change in the geometry close to the throat region. It must be emphasized that proper simulation requires the computed results to be one-dimensional. This has been achieved by keeping the nozzle wall slope very small, while at the same time the hub and tip radii are set to large values (their ratio is close to unity). An exact analytical solution can be obtained from compressible flow tables (one-dimensional). The pressure ratio $p_2/p_{01} = 0{\cdot}818$ produces high subsonic flow in the nozzle with maximum Mach number equal to 0·68. Figure 10 shows the comparison between the computed and analytically produced results. The agreement in the high-subsonic-flow region is satisfactory. A rapid change in the geometry near the throat region produced a steep change in the gradient of the Mach number, which has been correctly predicted by the proposed method. The value of the coefficient C_4 in the pressure correction ($\mathrm{pcor}_{i,j,k}$) equation (43) was set equal to 0·1. As mentioned, the value of C_4 is multiplied by the factor $1{\cdot}0 + \Delta\rho/\rho$. Outside the shock region, as in the current test case, the $\Delta\rho$-values are negligible.

Dawes '*thin–thick–thin*' *aerofoil*

Dawes[12] measured the surface pressure distributions on an NACA series 34 aerofoil with varying thickness across the span. The maximum and minimum thicknesses were chosen to be 12·0% and 6·0% of the blade chord respectively (NACA 006-34 and NACA 0012-34). The aerofoil used, shown in Figure 11, was uncambered, untwisted, of constant chord across the span and was mounted in the centreplane of a wind tunnel with solid parallel walls at 0° incidence. The thickness variation was designed to give subsonic flow over the thin part of the span and regions of supersonic flow elsewhere. The aerofoil was tested by Dawes under various exit flow conditions. It was made in order to assess the effects of the sidewall boundary layers on the aerofoil flow field. At midspan the aerofoil was of maximum thickness of 12·0% of the blade chord (thick), while at each of the two tips the maximum thickness was only 6·0% of the chord (thin). Diagrammatic aerofoil and working section arrangements are shown in Figure 12.

To perform the computational analysis, the grid mesh ($8 \times 56 \times 8$) was extended half a chord up and one chord downstream from the aerofoil leading and trailing edges respectively. Each blade pitch was equal to the width (164·0 mm) of the working space tunnel, while the blade span was 112·0 mm. Owing to the inherent symmetry of the thin–thick–thin blade and in order to save computing time, the span and pitch sizes actually used were only half of the above numbers. Thus the tested blade section was only one-quarter of the total available geometry.

Calculated results are compared directly with available measured values as well as with potential flow predictions.[13] Figures 13 and 14 show the comparison of the current method predictions against those using a fully 3D potential flow solver as well as with the measurements taken by Dawes. The comparison refers to the static p/p_{01} pressure ratios along the blade chord for the 6·0% (thin) and 12·0% (thick) sections of the blade respectively when the measured back pressure ratio p_2/p_{01} was equal to 0·69. The back pressure $p_2/p_{01} = 0{\cdot}66$ used for the calculation was chosen on purpose to produce the best agreement between prediction and measurements. The same was true for the potential flow prediction back pressure value, which was chosen to be 0·673. The current method produces diffusion rather than shock on the aerofoil surface, a result which is supported by the measurements but not by the potential flow solver predictions.

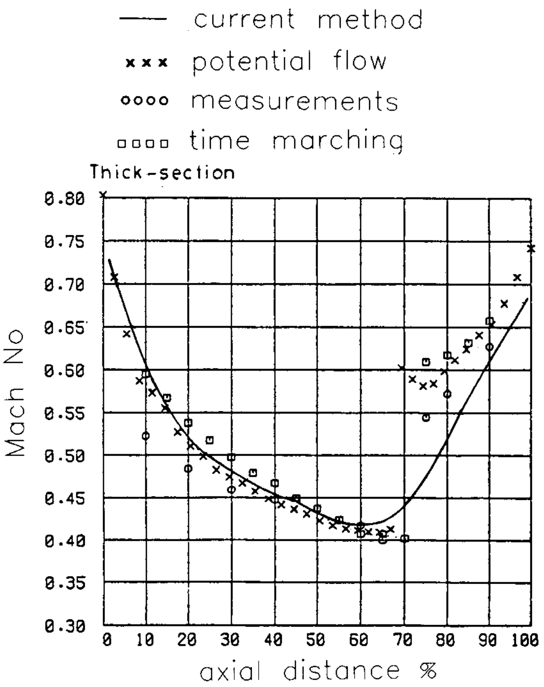

Figure 15. Comparison of blade pressure distribution between current method predictions, potential flow predictions, time-marching predictions and measurements on the thin section of the 'thin–thick–thin' aerofoil at measured $p_2/p_{01} = 0{\cdot}682$

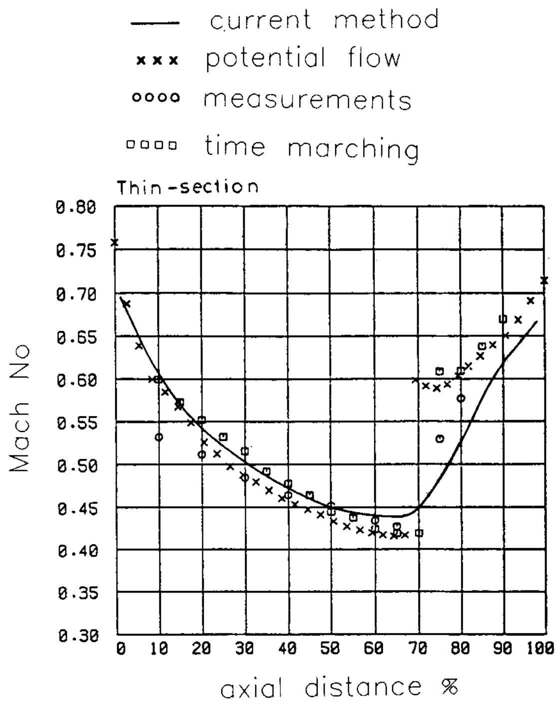

Figure 16. Comparison of blade pressure distribution between current method predictions, potential flow predictions, time-marching method predictions and measurements on the thick section of the 'thin–thick–thin' aerofoil at measured $p_2/p_{01} = 0{\cdot}682$

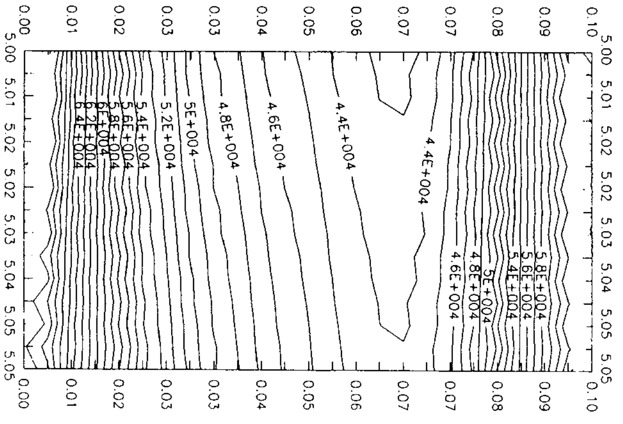

current method

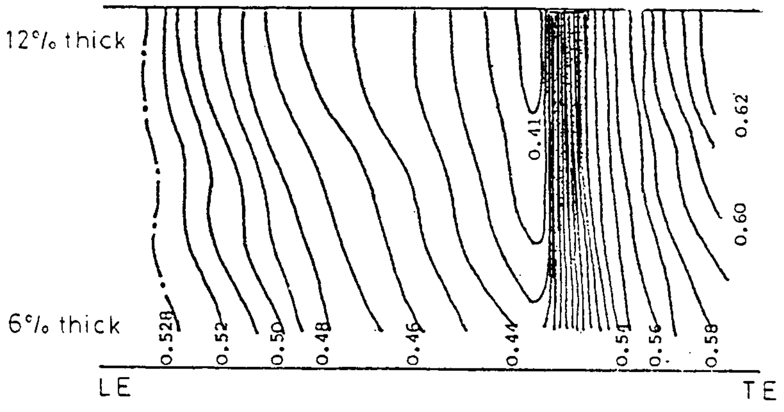

measurements

Figure 17. Comparison between measured and predicted isobars on the blade surface of the 'thin–thick–thin' aerofoil

The main reason for the apparent discrepancies between theory and measurements, particularly in the first 20·0% chord aerofoil surface flow region, is attributed to viscous flow behaviour of the flow due to reduced turbulence (small Reynolds number) in this back pressure region.[12]

Under higher-exit-flow conditions, when the experimental back pressure ratio was 0·682, a similar comparison is performed using $C_4 = 0{\cdot}2$ (equation (43)). However, the results of Denton's time-marching method are also incorporated. Figures 15 and 16 show all the above comparisons along the blade chord for the 6·0% (thin) and 12·0% (thick) sections of the blade respectively. The agreement between theories and experiment is satisfactory on either the 'thin' or the 'thick' blade sections. The disagreement between theories and experiment in the region downstream of the shock is due to viscous effects in the experiment. All predictions for the first 20·0% chord aerofoil surface flow region agree well with themselves but disagree with measurements, for the reasons stated earlier on.

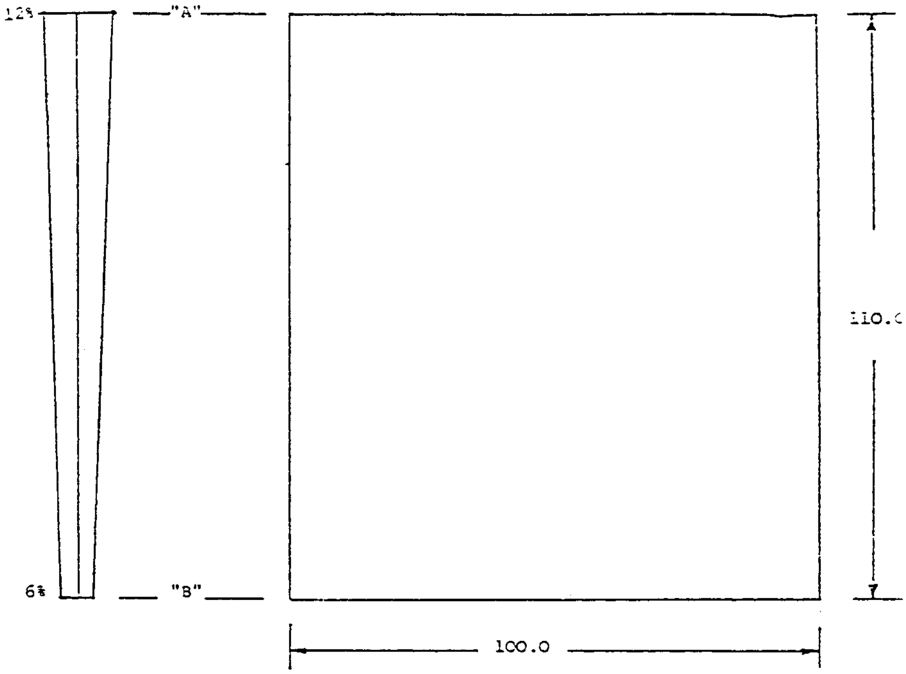

Figure 18. Dawes 'thin–thick' aerofoil and working section arrangements; all dimensions in millimetres

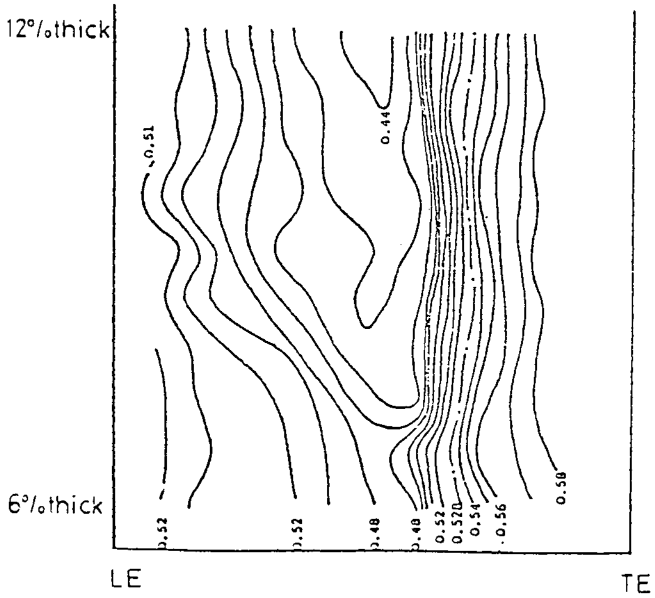

Figure 19. Measured isobars on the blade surface of the 'thin–thick' aerofoil at $p_2/p_{o1} = 0{\cdot}690$

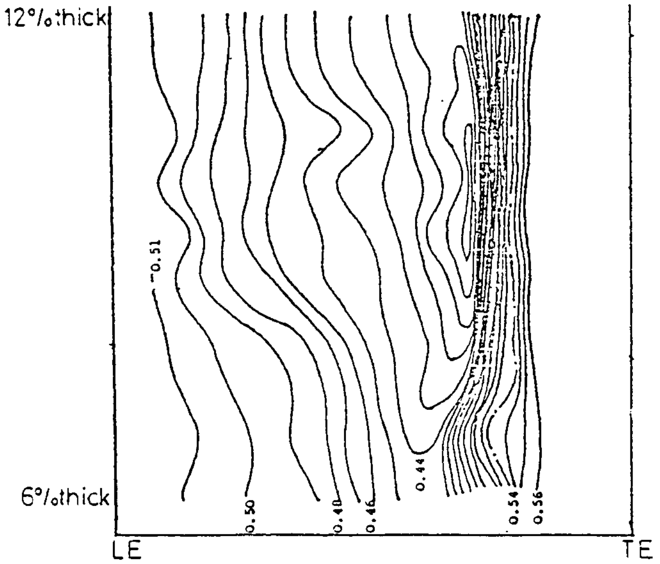

Figure 20. Measured isobars on the blade suface of the 'thin–thick' aerofoil at p_2/p_{o1} = 0·682

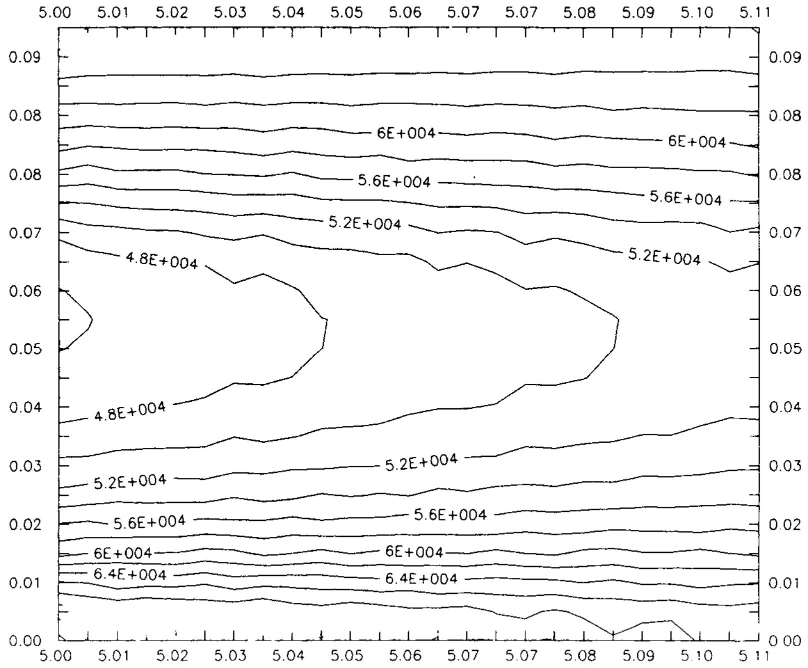

Figure 21. Current-method predicted isobars on the blade surface of the 'thin–thick' aerofoil at p_2/p_{o1} = 0·66

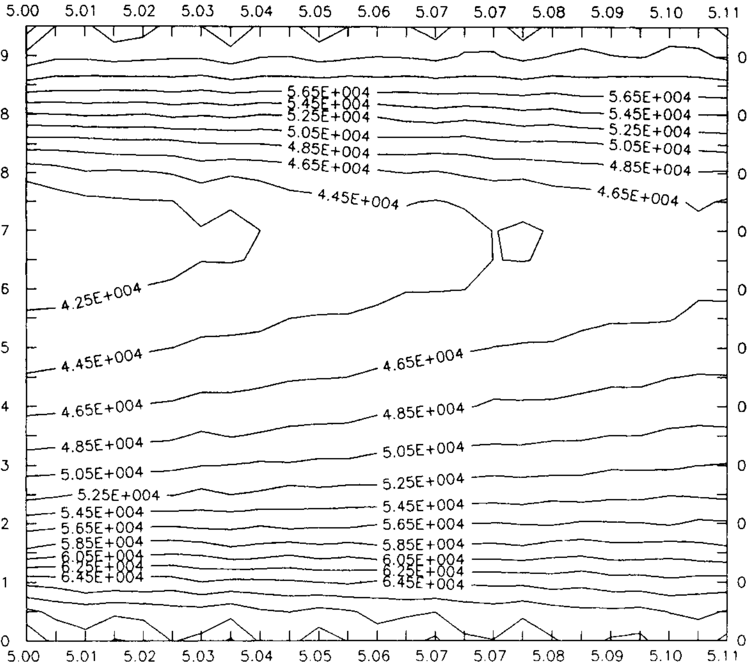

Figure 22. Current-method-predicted isobars on the blade surface of the 'thin–thick' aerofoil at $p_2/p_{01} = 0{\cdot}64$

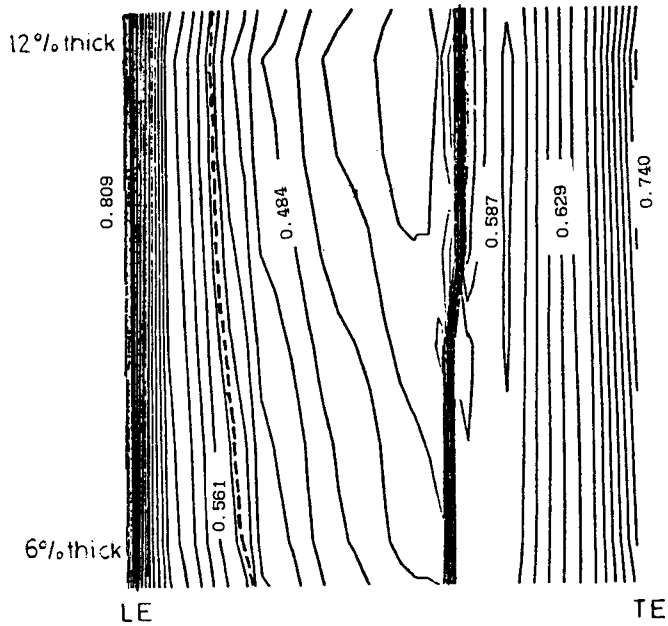

Figure 23. Potential-flow-predicted[13] isobars on the blade surface of the 'thin–thick' aerofoil at $p_2/p_{01} = 0{\cdot}669$

Measured and current-method-calculated isobars at measured p_2/p_{o1} = 0·682 are shown in Figure 17. All isobars tend to curve upwards when they reach the 'thick' section of the aerfoil, thus giving evidence of the 3D nature of the flow. The good agreement between theory and measurements all over the flow field is apparent. Note the locations of the sonic lines.

Dawes 'thin–thick' aerofoil

The aerofoil used, shown in Figure 11, is of the NACA series 34 with varying thickness across the span. The working section arrangement is shown in Figure 18. The blade span was again 110·0 mm. At one tip the blade thickness was 6·0% of the blade chord (thick), while at the other end the blade thickness has been increased to 12·0% of the blade chord (thick). Again each blade pitch was equal to the width (162 mm) of the working space tunnel. The thickness variation was designed to give subsonic flow over the thin part of the span and regions of supersonic flow elsewhere.

Reported measurements have been presented as contours of constant pressure plotted in the plane of the aerofoil. Two back pressure ratios have been tested, p_2/p_{o1} = 0·690 and 0·682, and the measured isobars are shown in Figures 19 and 20 respectively. Calculations were performed on a finite volume grid of 8 × 56 × 8 which was extended half a chord upstream and one chord downstream from the blade leading and trailing edges respectively. The calculations used C_4 = 0·4 and back pressure ratios p_2/p_{o1} = 0·66 and 0·64 which were lower than those measured in order to obtain the 'best' comparison. This was achieved by choosing the location of the shock wave to be located in the same place on the aerofoil as in the experiments. These results are shown in Figures 21 and 22 respectively. There is a significant 3D flow structure upstream from the shock wave, since the isobars are curved across the span, and this has been clearly

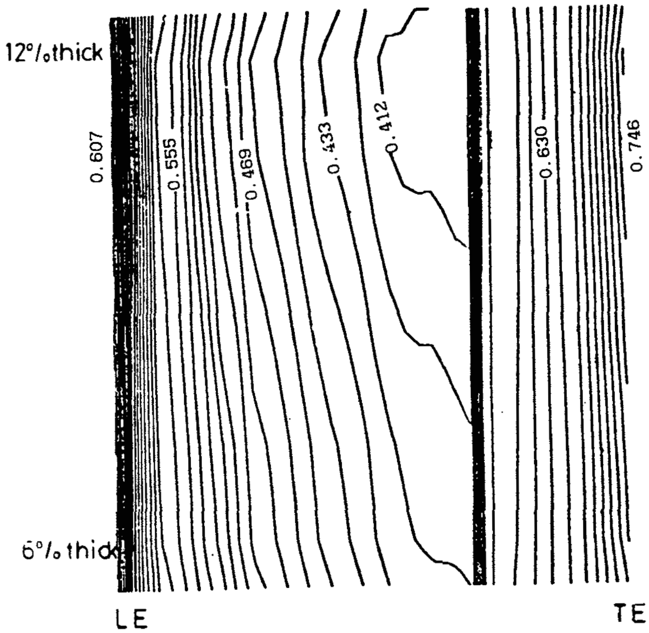

Figure 24. Potential-flow-predicted[13] isobars on the blade surface of the 'thin–thick' aerofoil at p_2/p_{o1} = 0·667

x/mm.	0	5	10	20	30	40	50	60	70	80	90	95	100
y/mm.	0	1.22	1.79	2.47	2.78	2.875	2.79	2.52	2.09	1.53	0.90	0.46	0.06

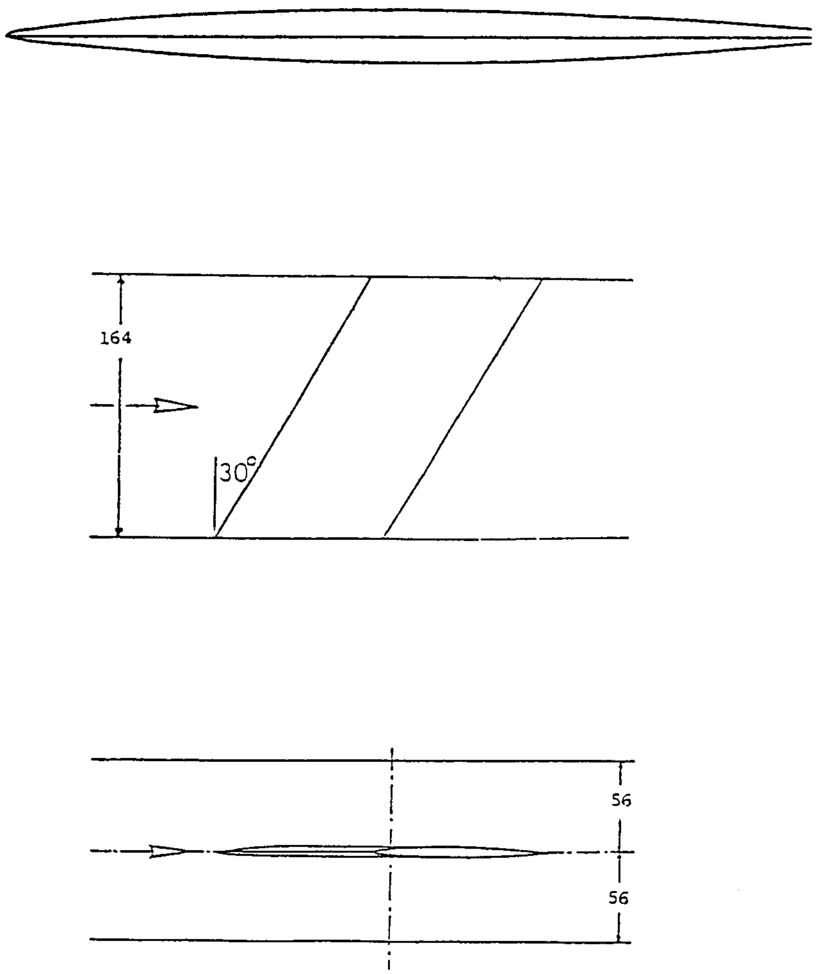

Figure 25. Dawes swept aerofoil and working section arrangements; all dimensions in millimetres

predicted by the method. The shock strength increases from the thin to the thick section of the aerofoil span. The shock strength and location are in very good agreement with the measurements. Finally, Figures 23 and 24 show the potential flow predictions for the above problem using $p_2/p_{01} = 0{\cdot}669$ and 0·667.

Dawes 30° swept aerofoil

The final test case was a swept aerofoil, also designed by Dawes, with chord and thickness constant across the span but swept at 30° between the working section sidewalls. The aerofoil geometry and working section arrangements are shown in Figure 25.

Contours of measured pressures are plotted in the plane of the aerofoil isobars at $p_2/p_{01} = 0{\cdot}621$ and are shown in Figure 26. Isobar contours are inclined towards the tip trailing edge, as

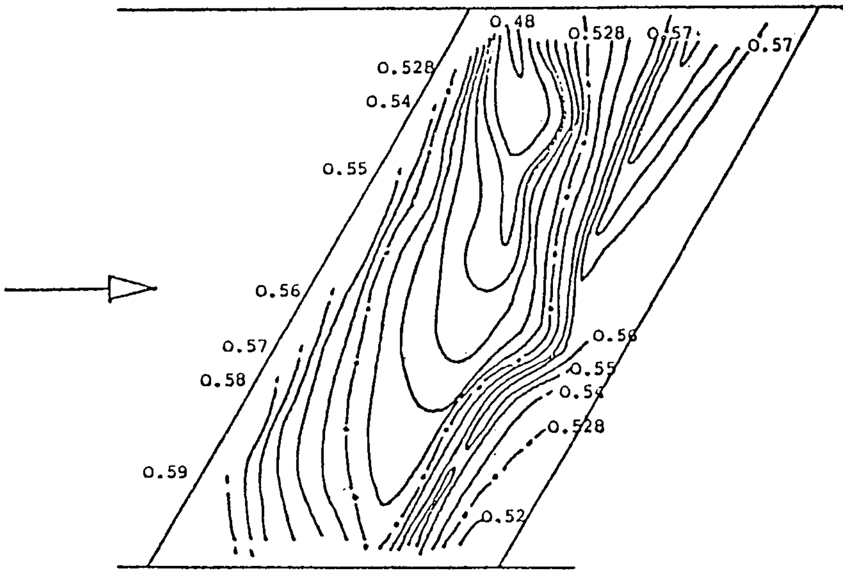

Figure 26. Measured isobars on the blade surface of the 30° swept aerofoil at $p_2/p_{o1} = 0{\cdot}621$

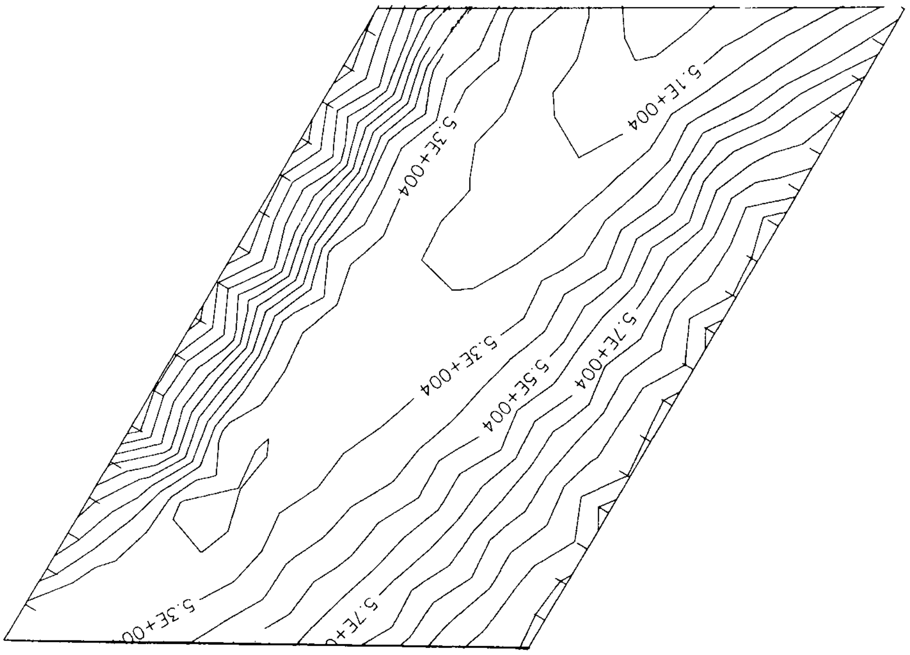

Figure 27. Current-method-predicted isobars on the blade surface of the 30° swept aerofoil at $p_2/p_{o1} = 0{\cdot}623$

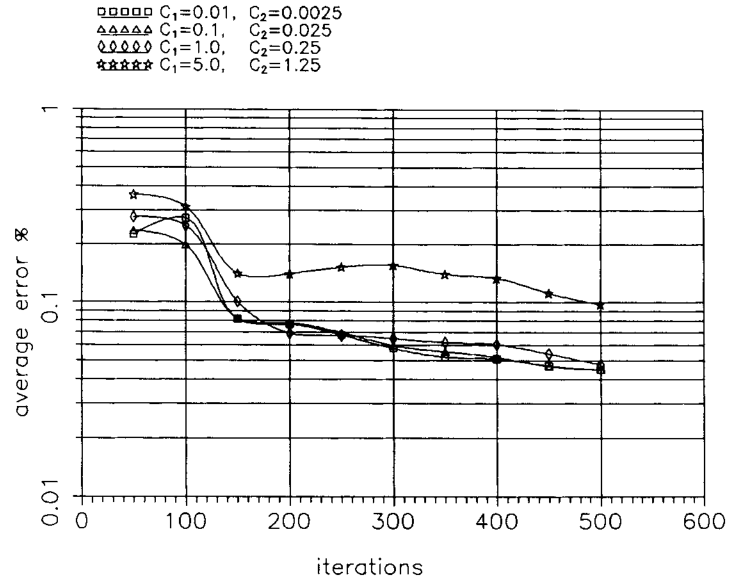

Figure 28. Convergence history for the 'thin–thick–thin' aerofoil using various values for the parameters C_1 and C_2

is clearly shown by measured and calculated results. The highest flow field Mach numbers are attained at the tip of the aerofoil very close to the blade leading edge region. An embedded transonic region extends from tip to root. Measured isobars also show the formation of another supersonic pocket at about 60·0% of the blade chord at the root section of the aerofoil. Calculated contours at $p_2/p_{o1} = 0{\cdot}623$ are shown in Figure 27.

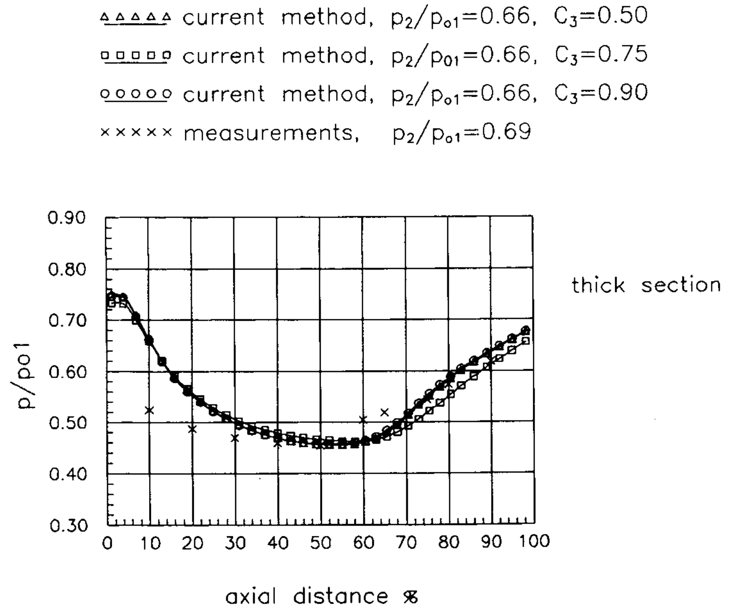

Figure 29. C_3 effects on the pressure ratio distribution along the axial distance of the thick section of the 'thin–thick–thin' aerofoil

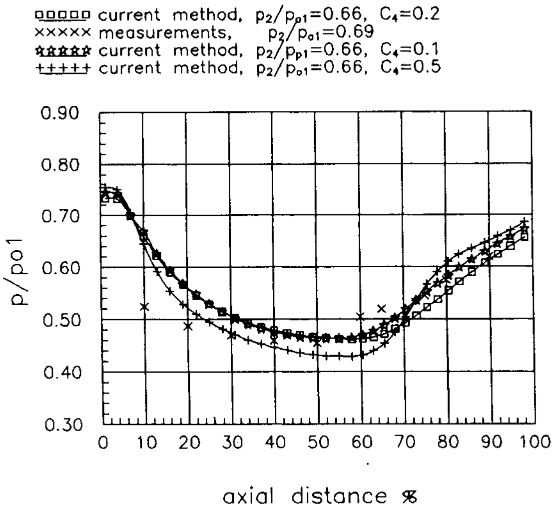

Figure 30. C_4 effects on the pressure ratio distribution along the axial distance of the thick section of the 'thin–thick–thin' aerofoil

An explanation of the flow field development round the swept aerofoil, also based on the calculated results, suggests that upstream from the aerofoil leading edge a pressure gradient is generated transverse to the incoming flow which increases the pressure upstream from the root leading edge region. This means that upstream from the tip leading edge region the flow must accelerate to maintain continuity. Thus the flow becomes faster near the tip than the root section of the aerofoil.

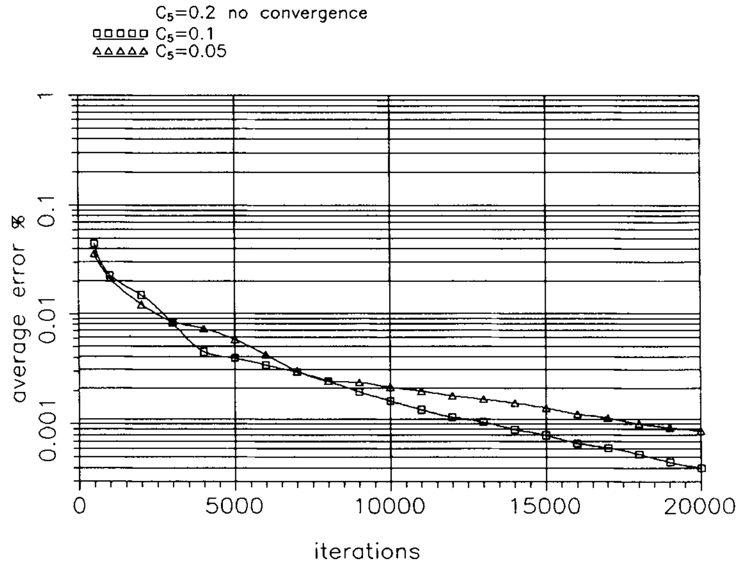

Figure 31. C_5 effects on the convergence history of the 'thin–thick–thin' aerofoil

ANALYSIS OF THE FACTORS C_1, C_2, C_3, C_4, C_5 AND C_6

The Dawes 'thin–thick–thin' aerofoil was chosen in order to demonstrate the performance of the various factors C_1, C_2, C_3, C_4, C_5 and C_6 used in the computations. Figure 28 shows the convergence history for the first 500 iterations using various C_1- and C_2-values, equations (38) and (40); of course, the solution has not yet converged (a full convergence history for the converging–diverging nozzle is shown in Figure 5 using $C_1 = 0{\cdot}1$ and $C_2 = 0{\cdot}025$). From Figure 28 it is evident that using high values of C_1 and C_2, the solution is slow in achieving convergence. The 'amplification' is more than enough and at even higher values the solution might not converge at all. The final solution is not affected by the choice of C_1 and C_2 (not shown).

Figure 29 shows the effects of C_3, equation (41), on the ratio p/p_{01} along the axial distance of the tested aerofoil section. The results refer to the thick section. Three values of C_3 are used, namely 0·50, 0·75 and 0·90. All computations performed in the current research work use 0·75. From Figure 29 it is evident that up to the 65·0% axial distance all three solutions are close to each other. From that region onwards a diffusion (shock) region is present and the three solutions show some differences from each other. The 0·50 and 0·90 solutions are very close one to another and both solutions are comparable with the measurements.

Figure 30 shows the effects of C_4, equation (43), on the pressure distribution over the thick section of the tested 'thin–thick–thin' aerofoil. The predicted results using $C_4 = 0{\cdot}5$ are close to the measured values, particularly in the high-diffusion region of the tested aerofoil. Predictions using $C_4 = 0{\cdot}2$, which is a typical value for the current tests, underestimate the pressure ratio in the diffusion region. At even higher C_4-values ($=1{\cdot}0$) the solution breaks down.

Figure 31 shows the effects on the convergence history using various C_5-values, equation (46). For the applied initial flow conditions a C_5-value of 0·2 failed to achieve convergence. Using $C_5 = 0{\cdot}1$, the solution converges faster (comparison is made against $C_5 = 0{\cdot}05$).

Finally, in Figure 32 the effects of using two different values (0·25 and 1·0) of C_6, equation (47), are shown. The final solution is not affected.

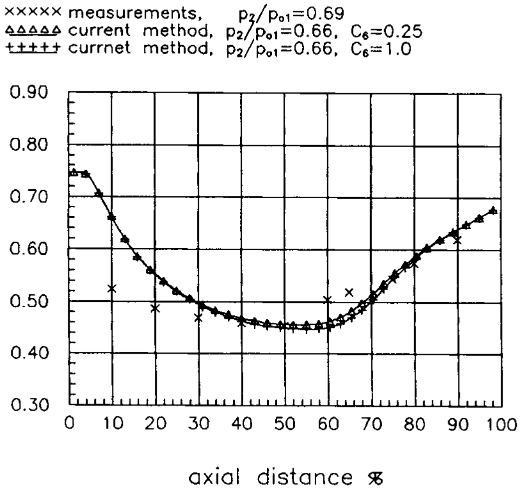

Figure 32. C_6 effects on the pressure ratio distribution along the axial distance of the thick section of the 'thin–thick–thin' aerofoil

CONCLUSIONS

An accurate and efficient numerical method for complex geometry turbomachinery blade rows has been developed. The code is based on a simple body-conforming grid system. It utilizes a simple time integration technique, while artificial viscosity is provided via a simple pressure correction formula. The programme has been tested on a variety of turbomachinery problems revealing 3D flow structure. Predictions for three 3D flows have been presented. Comparisons with measurements as well as with other numerical solutions demonstrate the accuracy and computational efficiency of the method. Main features of the flow are reasonably well predicted, even using comparatively coarse grids. However, much finer grids would be needed to resolve details of the complex leading and trailing edge flow regions. Whenever convergence problems have occurred, they have always been traced to bad grids and have vanished when the grid was refined. Future work will involve expanding the code to predict steady, three-dimensional, viscous flows in hydraulic machines (draft tubes, turbines, pumps).

REFERENCES

1. J. D. Denton, 'The calculation of three-dimensional viscous flow through multistage turbomachines', *ASME Paper 90-GT-19*, 1990.
2. C. Hirsch, *Numerical Computation of Internal and External Flows*, Vol. 2, Wiley, Chichester, 1990, Chap. 16, pp. 132–583.
3. J. D. Denton, 'A time-marching method for two-dimensional and three-dimensional blade to blade flows', *ARC R&D3775*, 1974.
4. C. F. Shieh and R. A. Delaney, 'An accurate and efficient Euler solver for three-dimensional turbomachinery flows', *ASME Paper 86-GT-200*, 1986.
5. K. F. Weber, D. W. Thoe and R. A. Delaney, 'Analysis of three-dimensional turbomachinery flows on C-type grids using an implicit Euler solver', *J. Turbomachinery*, **112**, 362–369 (1990).
6. T. Arts, 'Calculation of the three-dimensional steady inviscid flow in a transonic axial turbine stage', *ASME Paper 84- GT-76*, 1985.
7. D. G. Holmes and S. S. Tong, 'A three-dimensional Euler solver for turbomachinery blade rows', *ASME Paper 84- GT-79*, 1979.
8. J. V. Soulis, 'Finite-volume method for three-dimensional transonic potential flow through turbomachinery blade rows', *Int. J. Heat Fluid Flow*, **4**, (1983).
9. J. V. Soulis and K. V. Bellos, 'Conservation form of fluid dynamics equations in curvilinear coordinate systems, Part I, Mathematical analysis', *Tech. Chron. B*, **8**, (4), 69–97 (1988).
10. J. V. Soulis, 'A numerical method for subcritical and supercritical open channel flow calculation', *Int. j. numer. methods fluids*, in press.
11. J. D. Denton, 'Solution of Euler equations for turbomachinery flows, Part I: Basic principles and two-dimensional applications, Part II: Three-dimensional flows', *Proc. NATO Adv. Study Inst. on Thermodynamics and Fluid Mechanics of Turbomachines*, Izmir, 1984, pp. 2.2.1–2.2.29, 2.3.1–2.3.34.
12. W. N. Dawes, 'A study of shock waves in three-dimensional transonic flow', *Ph.D. Thesis*, Cambridge University, 1979.
13. J. V. Soulis, 'Calculation of transonic potential flow through turbomachinery blade rows', *Ph.D. Thesis*, Cambridge University, 1981.